Machine-learned search for the stable structures of silicene on Ag(111)

Yuji Hamamoto,[1,*] Thanh Ngoc Pham,[1] Malthe K. Bisbo,[2] Bjørk Hammer,[2] and Yoshitada Morikawa[1,3]
[1]*Department of Precision Engineering, Graduate School of Engineering, Osaka University, Suita, Osaka 565-0871, Japan*
[2]*Center for Interstellar Catalysis, Department of Physics and Astronomy, Aarhus University, DK-8000 Aarhus C, Denmark*
[3]*Research Center for Precision Engineering, Graduate School of Engineering, Osaka University, Suita, Osaka 565-0871, Japan*

(Received 26 July 2023; accepted 4 December 2023; published 21 December 2023)

The honeycomb lattice of silicene exhibits a variety of nontrivial reconstructions on the Ag(111) surface, whose diversity hampers the theoretical prediction of experimentally unidentified structures using computationally expensive density functional theory (DFT) calculations. We here apply an efficient method based on an evolutionary algorithm and a Gaussian process, which is trained on the fly with DFT calculations, to the search for the stable structures of silicene on Ag(111). We demonstrate that the structure search method can not only reproduce the well-known structures, but also predict the existence of metastable structures that are close in stability to the most stable ones. Detailed analyses of the obtained results reveal that such metastable structures play crucial roles in the stabilization of less ordered phases often observed experimentally. The present method can replace the conventional manual search based on intuition and is widely applicable to the investigations of new systems such as emerging two-dimensional materials.

DOI: 10.1103/PhysRevMaterials.7.124002

I. INTRODUCTION

Emerging two-dimensional materials have recently attracted much attention for their peculiar structural and electronic properties [1–5] as well as the potential applications to, e.g., electronics [6–8], spintronics [9–11], and energy devices [12–14]. In particular, silicene, a silicon analog of graphene, has been studied intensively in the last decade, because of its intriguing phenomena such as the quantum spin Hall effect [15,16], as well as better compatibility with current silicon-based electronics than graphene [17–19]. Whereas freestanding silicene is characterized by the alternately buckled honeycomb lattice [20–25], the buckling pattern is reconstructed when silicene is synthesized on a substrate. Scanning tunneling microscopy (STM) has revealed that silicene epitaxially grown on the Ag(111) surface, for example, exhibits a variety of reconstructions such as 4×4 [26–50], $\sqrt{13} \times \sqrt{13}R13.9^\circ$ [26,27,29–33,35–43,45,47,49,51,52], and $2\sqrt{3} \times 2\sqrt{3}R30^\circ$ [27,29,30,32,33,37,40,47,49,53–55] superstructures relative to the underlying Ag surface. They are further classified into several phases by the patterns of bright spots, whose underlying honeycomb lattice has also been visualized by atomic force microscopy (AFM) [56–61]. However, different phases are often observed simultaneously, and the blurred regions between them still indicate the existence of unidentified buckled structures.

Theoretically, stable structures of silicene on Ag(111) have been studied using the density functional theory (DFT) [62–73], but its application has been limited to the phases whose structures can be inferred from the STM and AFM images. This is because the structural diversity inherent to the buckling nature of silicene hampers DFT calculations covering all the possible buckled structures. To overcome the difficulty, we here resort to a machine-learned structure search using global optimization with first-principles energy expressions (GOFEE) [74–76]. This scheme not only allows for a global search based on an evolutionary algorithm (EA) but also accelerates the relaxation of the EA-generated candidates by using the lower confidence bound, $E - \kappa\sigma$, to the energy landscape, where energy E and its uncertainty σ are estimated by a Gaussian process (GP) and κ is a constant, typically 2. The GP is trained on the fly by DFT single-point calculations for the GP-relaxed structures, which is much cheaper than the complete relaxation by means of DFT calculations. To date, GOFEE has successfully predicted nontrivial structures of polycyclic aromatic hydrocarbons on graphene [77], ultrathin oxides on the $Pt_3Sn(111)$ surface [78], and freestanding and $CeO_2(111)$ supported PtO_x clusters [79]. In the present paper, we demonstrate that GOFEE is also applicable to the search for the stable structures of silicene on Ag(111). Our results include not only the well-known structures but also metastable ones that have received little attention so far. In particular, they include metastable structures that are close in stability to the most stable ones and can be observed experimentally. We propose the existence of such metastable structures as the origin of less-ordered phases often observed in the $\sqrt{13} \times \sqrt{13}R13.9^\circ$ and $2\sqrt{3} \times 2\sqrt{3}R30^\circ$ phases.

II. METHODS

The DFT calculations are carried out using the GPAW code [80,81] with the Perdew-Burke-Ernzerhof (PBE) exchange-correlation functional [82]. Spin-orbit or van der Waals

*Corresponding author: hamamoto@prec.eng.osaka-u.ac.jp

interactions are not taken into account. We explore the stable structures of silicene on Ag(111) in two steps, using a double-zeta polarized basis set for the linear combination of atomic orbitals (LCAO) and a plane-wave (PW) basis set with a cutoff energy of 400 eV, respectively. The lattice constant of bulk Ag is calculated to be 4.15 Å for both methods. Note that the calculated result is 1.5% larger than the experimental value of 4.06 Å estimated at zero temperature [83,84], which is due to the repulsive nature of the PBE exchange functional.

We first apply GOFEE to silicene on Ag(111) within the LCAO method. The Ag(111) surface is modeled with a fixed slab composed of a single layer of Ag atoms and a vacuum layer of 10 Å. To realize silicene with a small mismatch to Ag(111), we focus on the 4×4, $\sqrt{13} \times \sqrt{13}$, $2\sqrt{3} \times 2\sqrt{3}$, and $\sqrt{7} \times \sqrt{7}$ supercells, in which 18, 14, 14, and 8 Si atoms, respectively, are allowed to move within 4 Å above the surface. In the surface Brillouin zone (BZ), 6×6 k points are sampled for the $\sqrt{7} \times \sqrt{7}$ supercell, while 4×4 k points are sampled for the others. Fifty independent GOFEE searches are performed in order to obtain a set of stable structures for each system. We then switch to the PW method to fully relax the structures obtained by GOFEE. Two Ag layers are added to the bottom of each stable structure, and the whole system is relaxed until the atomic forces fall below 0.08 nN (0.05 eV/Å), except for the atoms in the bottom layer, which are fixed at the bulk positions.

It should be noted that the above procedure implicitly assumes that silicene is grown on a nearly flat Ag(111) surface, whereas prior DFT calculations have suggested the possibility for Si atoms to penetrate the topmost Ag layer owing to the excess energy released upon adsorption [85]. On the other hand, *ab initio* molecular dynamics (AIMD) simulations have revealed that the honeycomb structure of silicene is preserved on Ag(111) below 800 K without forming a silicide-like layer. Thus, we expect that the results obtained with the present approach correspond to the structures experimentally realized under such a temperature condition.

The band structures of silicene on Ag(111) and the k-resolved density of states (DOS) projected onto the silicene layer are calculated using the STATE code [86–88] with the norm-conserving pseudopotentials. [89]. The plane-wave basis set is used to expand wave functions (charge density) with a cutoff energy of 64 Ry (400 Ry). The other computational conditions are the same as the PW method of GPAW except for the geometries of the systems, which are fixed to the relaxed structures obtained above.

III. RESULTS AND DISCUSSION

A. Geometric structures

We here present the stable structures of silicene on Ag(111) obtained by GOFEE. It should be noted that, on the Ag three-layer slab, two similar but inequivalent structures of silicene are possible that differ only by the positions of the fcc- and hcp-hollow sites of the Ag surface. In what follows, we show only the more stable one of each pair unless otherwise noted, since the energy difference is negligibly small.

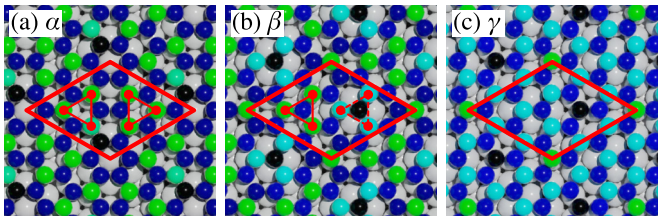

FIG. 1. Schematic views of the $4 \times 4{-}\alpha$ (a), β (b), and γ (c) structures. The heights of Si atoms are represented by a color gradient that ranges from green (highest) to cyan, blue, and black (lowest).The underlying Ag atoms are depicted with gray spheres. The rhombus shows the unit cell in each system, while the triangles indicate trimer protrusions. In panel (b), the trimer indicated by the dashed triangle is lower than that indicated by the solid triangle.

1. The 4×4 *structures*

We begin with the 4×4 structures [26–50,56–65, 67–72,90–95], since they have been well studied so far, and can play the role of a benchmark of GOFEE for predicting the stable structures of silicene on Ag(111). The results for the 4×4 structures are shown in Fig. 1, where the representative ones with a honeycomb lattice are depicted. The heights of Si atoms are represented by a color gradient that ranges from green (highest), to cyan, blue, and black (lowest), while the underlying Ag atoms are depicted with gray balls. We compare the stabilities of different structures using the formation energy per Ag(111)-(1×1) unit cell

$$E_{\mathrm{form}} = \frac{1}{N_{\mathrm{Ag}}^{\mathrm{layer}}}(E_{\mathrm{Si/Ag}} - E_{\mathrm{Ag}} - N_{\mathrm{Si}}\varepsilon_{\mathrm{Si}}), \tag{1}$$

where $E_{\mathrm{Si/Ag}}$, E_{Ag}, and $\varepsilon_{\mathrm{Si}}$ denote the total energies of silicene on Ag(111), a clean Ag(111) surface, and bulk Si per atom, respectively, while N_{Si} is the number of Si atoms forming silicene and $N_{\mathrm{Ag}}^{\mathrm{layer}}$ is the number of Ag atoms per slab layer. The buckled structure in Fig. 1(a) is characterized by two trimer protrusions in opposite orientations, and the protruded Si atoms are higher than the others by about 0.8 Å. The structure has a formation energy of 0.187 eV, which is the smallest of the three structures in Fig. 1. Thus the structure can be assigned to the $4 \times 4{-}\alpha$ structure, one of the most commonly observed phases in silicene on Ag(111).

The buckled structure in Fig. 1(b) has a monomer protrusion at the cell corner and two trimer protrusions in the same orientation. The right trimer is lower than the others by about 0.3 Å, which suggests that the structure is characterized by a Y-shaped pattern due to the other protrusions. Indeed, a similar pattern has been theoretically predicted as a metastable structure [64,65], and also been experimentally observed in a boundary between two $4 \times 4{-}\alpha$ domains [36,48], which is referred to as the $4 \times 4{-}\beta$ phase. This is consistent with the fact that the $4 \times 4{-}\beta$ structure has a slightly larger formation energy of 0.198 eV. Note that the trimer protrusions in Fig. 1(b) have approximately threefold symmetry, whereas in the metastable structure predicted in Refs. [64,65], one of the three Si atoms is lower than the others by about 0.7 Å, breaking the threefold symmetry.

In addition to the $4 \times 4{-}\alpha$ and β structures, our results also include another metastable structure as shown in

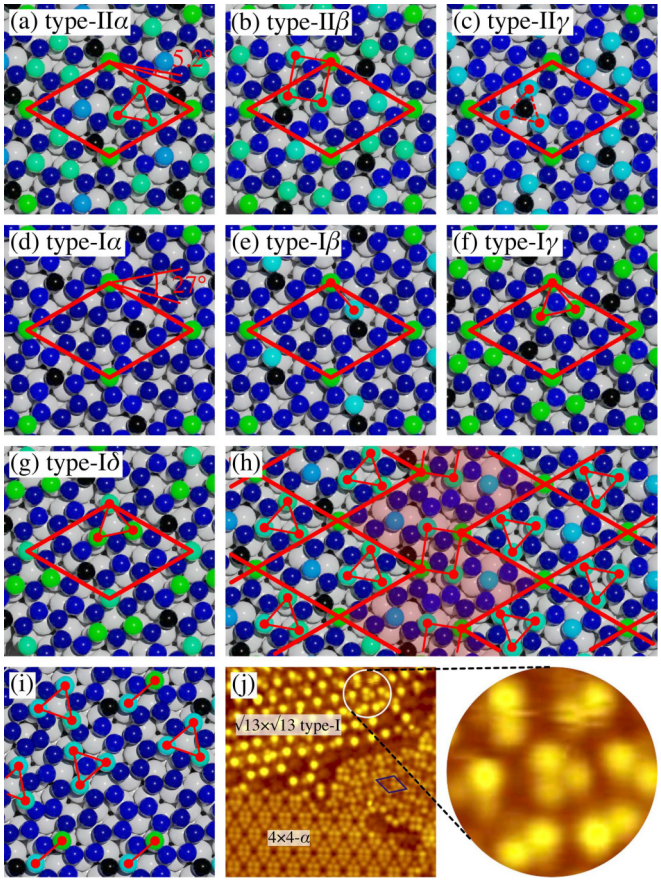

FIG. 2. Schematic views of the $\sqrt{13} \times \sqrt{13}$ type-II (a)–(c) and type-I (d)–(g) structures. The color schemes for the Si and Ag atoms are the same as those in Fig. 1. The rhombus shows the unit cell in each system, while the line segment, triangle, and rectangle indicate dimer, trimer, and tetramer protrusions, respectively. In panel (c), the trimer indicated by the dashed triangle is lower than the protrusion at the cell corner. Panel (h) shows two type-IIα domains separated by a line defect composed of tetramer protrusions, which is indicated by a shaded region. Panels (i) and (j) show a comparison between a model of the less-ordered structures constructed from type-Iβ, γ, and δ structures and the STM image taken from Ref. [36]. In the latter, we have added labels of phases and an enlarged view of the T phase.

Fig. 1(c), which we refer to as the $4 \times 4{-}\gamma$ structure. The structure is almost alternately buckled by about 1 Å just as freestanding silicene [20–25], except for the protrusion (dent) at the Si atom located on the top (hcp-hollow) site. The similarity suggests the emergence of Dirac electrons with a small energy gap in the $4 \times 4{-}\gamma$ structure, whose possibility will be discussed in Sec. III C. To the best of our knowledge, the $4 \times 4{-}\gamma$ structure has never been reported so far, but the structure is expected to be rarely observed experimentally because of an even larger formation energy of 0.228 eV.

2. The $\sqrt{13} \times \sqrt{13}$ structures

We next investigate the $\sqrt{13} \times \sqrt{13}$ structures [26,27,29–33,35–43,45,47,49,51,52,56,57,59–65,69,72,90,92–95], which are often observed together with the $4 \times 4{-}\alpha$ structure. The results for the $\sqrt{13} \times \sqrt{13}$ structures are shown in Fig. 2, where the structures in Figs. 2(a)–2(c) [2(d)–2(g)] can be classified into type-II (I) according to an angle of $\theta = 5.2°$ (27°) between the Si[110] and Ag[110] directions [27]. The buckled structure in Fig. 2(a) has a monomer protrusion at the cell corner and a trimer protrusion enclosing the hcp-hollow site. There is another protrusion in the left half, which is lower than the others by about 0.5 Å. The structure has a formation energy of 0.200 eV, which is the smallest of the structures in Fig. 2, and can be assigned to the structure often referred to simply as the $\sqrt{13} \times \sqrt{13}R13.9°$ type-II phase [27].

The buckled structure in Fig. 2(b) is characterized by a tetramer protrusion at the cell corner, and has a slightly larger formation energy of 0.204 eV. A similar tetramer protrusion has been theoretically predicted as a metastable structure [64,65], and also been experimentally observed in a boundary between two $\sqrt{13} \times \sqrt{13}$ domains that are similar to Fig. 2(a) but rotated 180° relative to each other [36,51,52,59,61]. Moreover, $\sqrt{13} \times \sqrt{13}$ domains displaying tetramer protrusions have also been identified by high-resolution AFM [59]. For distinction, we here refer to the structure in Fig. 2(a) [2(b)] as the $\sqrt{13} \times \sqrt{13}$ type-IIα (β) structure. Note that the 180° rotation converts the type-IIα structure to a slightly less stable one as shown on the right-hand side of Fig. 2(h), in which the trimer encloses the fcc-hollow site. Figure 2(h) also shows a line defect between the two type-IIα domains, where tetramer protrusions are analogous to those in Fig. 2(b). Here the type-IIβ structure acts as a boundary between two inequivalent domains unlike the $4 \times 4{-}\beta$ structure mentioned in Sec. III A 1, which appears in a boundary between two equivalent $4 \times 4{-}\alpha$ domains.

Our results also include another type-II structure shown in Fig. 2(c), which we refer to as the type-IIγ structure. The buckled structure is characterized by a monomer protrusion at the cell corner and a trimer protrusion in a half unit cell, and can be confused with the type-IIα structure. However, the type-IIγ structure is expected to be rarely observed experimentally, since the structure is the most unstable of the structures in Fig. 2 with a formation energy of 0.222 eV.

The buckled structures in Figs. 2(d)–2(f) are similar to each other except for the protrusions at the cell corners, which are monomer, dimer, and trimer protrusions, respectively. In addition, the structure in Fig. 2(g) also shows a trimer protrusions. These four structures, which we refer to as type-Iα, β, γ, and δ structures, have similar formation energies of 0.208, 0.209, 0.214, and 0.215 eV, respectively, and can be observed simultaneously. Indeed, the $\sqrt{13} \times \sqrt{13}R13.9°$ type-I phase has been observed experimentally as hexagonally packed protrusions, some of which are round while others are elongated in random orientations [29,30,33,35,36,41]. Such a less-ordered structure is often referred to as the T (or dotted) phase [29]. Although an Si monomer [36,51,62,69,95] [Fig. 2(d)] and an Si hexagonal ring [27,30,60] have been proposed as the models of the round protrusion, the origin of the T phase is yet to be fully understood. Our results indicate that the less-ordered structure of the T phase can be attributed to the coexistence of the monomer (type-Iα), dimer (type-Iβ), and trimer (type-Iγ and δ) protrusions. The structural models for the type-Iα, γ, and δ structures have already been proposed [38,62,95], while the type-Iβ structure has never been reported despite the experimental observation of elongated protrusions. In Fig. 2(i), we construct an example of the less-ordered structure from the

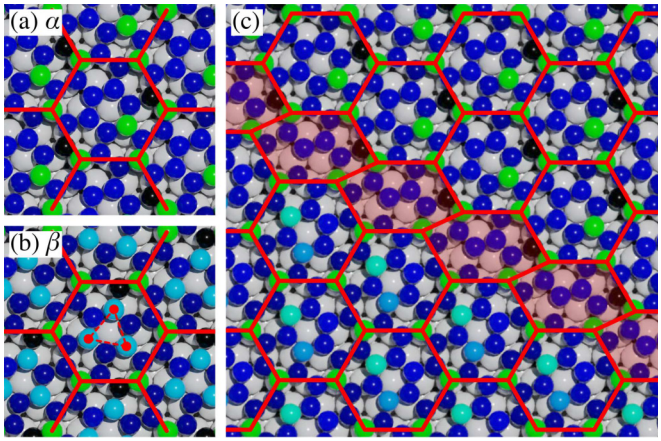

FIG. 3. Schematic views of the $2\sqrt{3} \times 2\sqrt{3}$−$\alpha$ (a) and β (b) structures. The color schemes for the Si and Ag atoms are the same as those in Fig. 1. In panels (a) and (b), the hexagonal pattern shows the large honeycomb lattice formed by the protrusions. In panel (b), the trimer protrusion indicated by the dashed triangle is lower than the honeycomb protrusion. Panel (c) shows two $2\sqrt{3} \times 2\sqrt{3}$−$\alpha$ domains separated by a line defect due to a contraction of the large honeycomb lattice, which is indicated by a shaded region.

type-Iβ, γ, and δ structures, which is analogous to the STM image with dimer and trimer protrusions [29,36] as shown in Fig. 2(j).

3. The $2\sqrt{3} \times 2\sqrt{3}$ structures

The results for the $2\sqrt{3} \times 2\sqrt{3}$ structures [27,29,30,32,33,37,40,47,49,53–55,61–65,69,72,92,93,95,96] are shown in Fig. 3. The buckled structures in Figs. 3(a) and 3(b) are both characterized by the protrusions forming a large honeycomb lattice but differ in the structures inside the hexagonal rings. Namely, the additional protrusion in a hexagon of Fig. 3(a) breaks the rotational symmetry, whereas the trimer protrusion in that of Fig. 3(b), which is lower than the large honeycomb lattice by about 0.5 Å, almost preserves the threefold symmetry. We refer to the structure in Fig. 3(a) [3(b)] as the $2\sqrt{3} \times 2\sqrt{3}$−$\alpha$ (β) structure. The two structures have close formation energies of 0.208 and 0.211 eV, respectively, and it has also been shown that the relative stability is reversed when a van der Waals density functional (vdW-DF) [97,98] is adopted [69]. These results suggest that the two structures have similar stabilities and can be observed simultaneously. Experimentally, the STM measurements have revealed that the $2\sqrt{3} \times 2\sqrt{3}$ phase exhibits a moiré-like pattern composed of ordered and disordered regions. Based on a simple model, Jamgotchian *et al.* have attributed the disorder to an apparent contraction of the large honeycomb lattice due to the relaxation of silicene [55]. Figure 3(c) shows the contracted large honeycomb lattice as a line defect between two $2\sqrt{3} \times 2\sqrt{3}$−$\alpha$ domains. It should be noted that the monomer protrusion inside the hexagon of the $2\sqrt{3} \times 2\sqrt{3}$−$\alpha$ plays the role of a lattice point in the contracted large honeycomb lattice, facilitating the creation of line defects. This indicates that the disorder observed in the $2\sqrt{3} \times 2\sqrt{3}$ phase originates from the coexistence of the $2\sqrt{3} \times 2\sqrt{3}$−$\alpha$ and β structures.

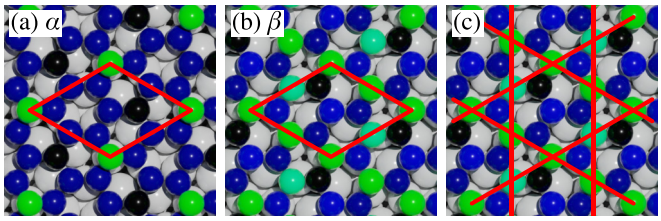

FIG. 4. Schematic views of the $\sqrt{7} \times \sqrt{7}$−α (a) and β (b) structures. The color schemes for the Si and Ag atoms are the same as those in Fig. 1. In panels (a) and (b), the rhombus shows the unit cell in each system. In panel (c), the lines show the large kagome lattice formed by the protrusions in panel (b).

4. The $\sqrt{7} \times \sqrt{7}$ structures

We finally investigate the $\sqrt{7} \times \sqrt{7}$ structures [30,62,69], the observation of which has never been reported except for the STM measurements by Chiappe *et al.* [30]. It should be noted that a similar phase can also be seen in the STM image by Resta *et al.* [57] as pointed out in Ref. [69]. The buckled structure in Fig. 4(a) has a monomer protrusion at the cell corner, while the other part of the honeycomb lattice is almost flat and lower than the former by about 1 Å. Thus the structure is essentially the same as that obtained by vdW-DF [69] but differs from the flat structure originally proposed in Ref. [27]. The buckled structure in Fig. 4(b) is characterized by the large kagome lattice formed by the protrusions as shown in Fig. 4(c). A similar kagome pattern has also been predicted in Ref. [62], but the in-plane position of silicene relative to the Ag surface is different from the GOFEE result in Fig. 4(b), where the hexagonal rings enclose either a top or a bridge site. We refer to the structures in Figs. 4(a) and 4(b) as the $\sqrt{7} \times \sqrt{7}$−α and β structures, respectively. The former has a formation energy of 0.205 eV, while the latter has a much larger formation energy of 0.243 eV and the corresponding kagome lattice is expected to be rarely observed experimentally. This is consistent with the fact that hexagonally packed round protrusion corresponding to the $\sqrt{7} \times \sqrt{7}$−α structure has been observed in the STM image [30].

5. Summary of the structure search

As seen above, the structure search based on GOFEE has reproduced successfully the well-known stable structures such as 4×4−α [Fig. 1(a)], $\sqrt{13} \times \sqrt{13}$ type-IIα [Fig. 2(a)], and $2\sqrt{3} \times 2\sqrt{3}$−$\beta$ [Fig. 3(b)] structures, and also generated metastable ones, some of which can be considered as new findings revealed by GOFEE. For example, the 4×4−γ structure with the almost alternately buckling pattern [Fig. 1(c)] and the $\sqrt{7} \times \sqrt{7}$−β structure characterized by the large kagome lattice [Fig. 4(b)] are interesting from a structural point of view, although these structures are expected to be rarely observed due to the large formation energies. On the other hand, the $\sqrt{13} \times \sqrt{13}$ type-Iβ structure with the dimer protrusion [Fig. 2(e)] is close in stability to the other $\sqrt{13} \times \sqrt{13}$ type-I structures already proposed [Figs. 2(d), 2(f), and 2(g)], and is analogous to the elongated protrusion observed in the T phase. The $2\sqrt{3} \times 2\sqrt{3}$−$\alpha$ structure characterized by the large honeycomb lattice with the monomer protrusion

[Fig. 3(a)] has been pointed out only in the vdW-DF study [69] and received little attention. However, our results obtained with the PBE functional predicts that the $2\sqrt{3}\times 2\sqrt{3}$–$\alpha$ structure coexists with the well-known $2\sqrt{3}\times 2\sqrt{3}$–$\beta$ structure, and the importance of the former can be confirmed by its higher compatibility with a line defect than the latter. Thus our results demonstrate that GOFEE is useful not only for identifying the most stable structures, but also for understanding less-ordered phases due to the coexistence of metastable structures.

B. Stoichiometry dependence

A striking feature of silicene on Ag(111) is the fact that phases with different stoichiometries are often observed simultaneously. To examine the influence of the stoichiometry on the stabilities of the structures obtained above, we now modify Eq. (1) to yield the surface free energy with respect to Si's chemical potential μ_{Si} as

$$\Omega \simeq \frac{1}{N_{\mathrm{Ag}}^{\mathrm{layer}}}(E_{\mathrm{Si/Ag}} - E_{\mathrm{Ag}} - N_{\mathrm{Si}}\mu_{\mathrm{Si}}), \tag{2}$$

where the contributions from the entropy and pressure have been neglected [99]. In Fig. 5(a), we plot $\Delta\Omega \equiv \Omega - \Omega_{4\times4\text{-}\alpha}$ as a function of $\Delta\mu_{\mathrm{Si}} \equiv \mu_{\mathrm{Si}} - \varepsilon_{\mathrm{Si}}$, with $\Omega_{4\times4\text{-}\alpha}$ being the surface free energy of the 4×4-α structure. In this definition, $\Delta\mu_{\mathrm{Si}} > 0$ (<0) corresponds to an Si-rich (poor) condition relative to the chemical equilibrium with bulk Si. Figure 5(a) shows that the most stable phases under the Si-poor, Si-rich, and intermediate conditions are the $\sqrt{13}\times\sqrt{13}$ type-IIα, $2\sqrt{3}\times2\sqrt{3}$-α, and 4×4-α structures, respectively. These results are similar to those of previous studies [69,72], although there are some differences. For example, the phase boundary between the 4×4-α and $2\sqrt{3}\times2\sqrt{3}$-α structures appears at $\Delta\mu_{\mathrm{Si}} = 0.51$ eV in good agreement with the results for AIMD simulations with the PBE functional [72], whereas the other phase boundary at $\Delta\mu_{\mathrm{Si}} = -0.27$ eV is significantly higher than the AIMD result. The discrepancy is due to the fact that, regarding the $\sqrt{13}\times\sqrt{13}R13.9^\circ$ phase, AIMD has been applied only to a type-I structure with $\theta = 27^\circ$. This is geometrically different from the $\sqrt{13}\times\sqrt{13}$ type-IIα structure with $\theta = 5.2^\circ$, which is the most stable at low $\Delta\mu_{\mathrm{Si}}$ in the vdW-DF result [69] as well as in ours. It should be noted that the line of the 4×4-α structure intersects with those of the $\sqrt{13}\times\sqrt{13}$ type-I structures at chemical potentials ranging from $\Delta\mu_{\mathrm{Si}} = -0.58$ to -0.43 eV in Fig. 5(a), which are closer to the boundary between the 4×4 and $\sqrt{13}\times\sqrt{13}R13.9^\circ$ phases in Ref. [72]. Although the stabilization of the $\sqrt{13}\times\sqrt{13}$ type-IIα structure under the Si-poor condition in Fig. 5(a) is qualitatively consistent with the vdW-DF result [69], the boundary with the 4×4 phase appears at a significantly higher chemical potential of $\Delta\mu_{\mathrm{Si}} = 0.07$ eV in the latter. More importantly, the $\sqrt{7}\times\sqrt{7}$ structures are always metastable in Fig. 5(a), whereas the vdW-DF results predict that the $\sqrt{7}\times\sqrt{7}$-α structure becomes the most stable in a small range from $\Delta\mu_{\mathrm{Si}} = 0.47$ to 0.55 eV. These differences indicate that vdW-DF,

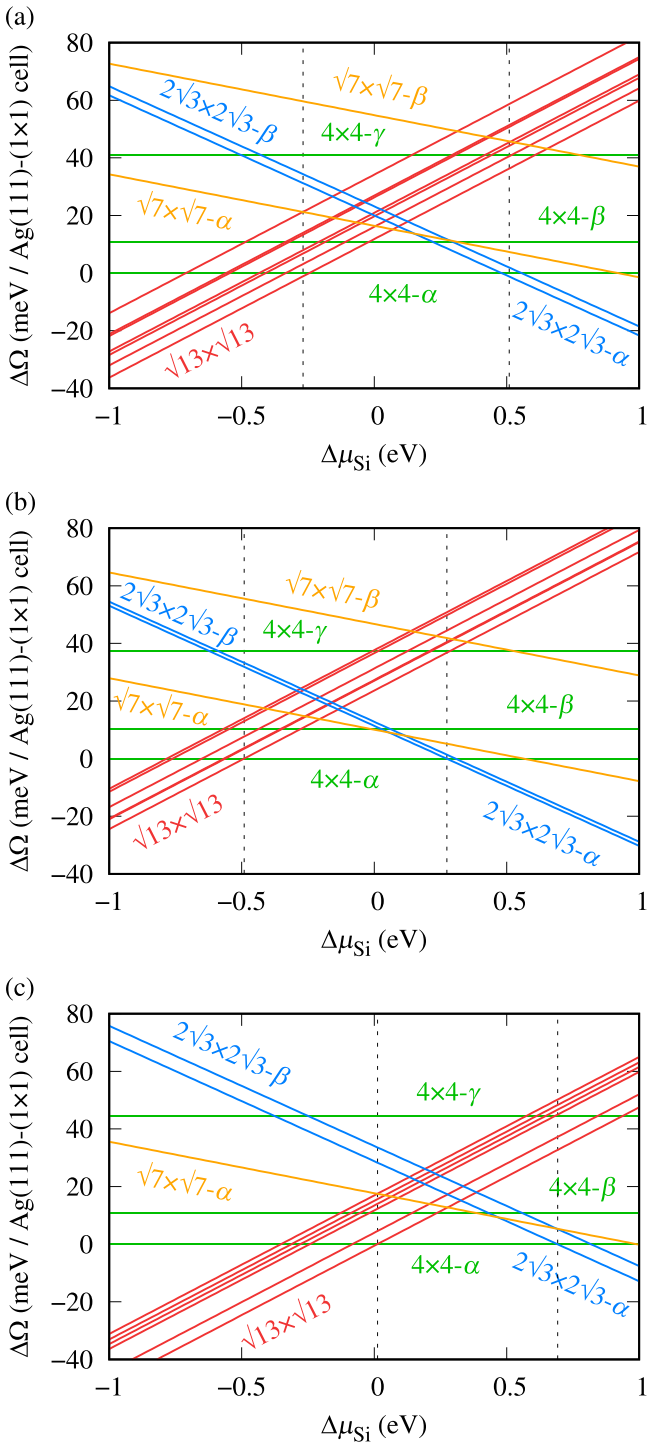

FIG. 5. Phase diagram of silicene on the Ag(111) surface without strain (a), and those with biaxial tensile (b) and compressive (c) strains of ±1%. The surface free energy (2) of each structure is plotted as a function of the chemical potential of Si, where the former is relative to the surface free energy of the 4×4-α structure and the latter is relative to the chemical potential of bulk Si. In panel (a), the seven lines for the $\sqrt{13}\times\sqrt{13}$ structures correspond to type-IIα, β, Iα–δ, and IIγ from bottom to top. In panel (b) [(c)], the six lines for the $\sqrt{13}\times\sqrt{13}$ structures correspond to type-IIα, β, Iα, β, δ, and γ (type-IIα, β, and Iα–δ) from bottom to top.

especially the optB86b-vdW functional, tends to stabilize the $\sqrt{13} \times \sqrt{13}R13.9^\circ$ type-IIα and $\sqrt{7} \times \sqrt{7}R19.1^\circ$ phases as compared with others. It should be noted that vdW interaction plays a minor role in these differences, because the stability of a superstructure is mainly determined by the covalent bonds between silicene and Ag(111) as well as the buckled structure of silicene.

In addition to the prediction of the most stable phases, Fig. 5(a) also provides useful insights into the metastable ones. For example, the 4×4-β structure is less stable than the 4×4-α structure by 11 meV and the second most stable only in the small range of -0.04 eV $\leqslant \Delta\mu_{\mathrm{Si}} \leqslant 0.24$ eV. In contrast, the $\sqrt{13} \times \sqrt{13}$ type-IIβ ($2\sqrt{3} \times 2\sqrt{3}$-$\beta$) structure is less stable than the $\sqrt{13} \times \sqrt{13}$ type-IIα ($2\sqrt{3} \times 2\sqrt{3}$-$\alpha$) structure only by 1 (3) meV, and always the second most stable for $\Delta\mu_{\mathrm{Si}} \leqslant -0.36$ ($\geqslant 0.58$) eV. This explains why the 4×4-α phase is experimentally observed as an almost ordered structure, while the $\sqrt{13} \times \sqrt{13}R13.9^\circ$ type-II and $2\sqrt{3} \times 2\sqrt{3}R30^\circ$ phases exhibit less ordered structures with domain boundaries. Moreover, the $\sqrt{13} \times \sqrt{13}$ type-Iα–δ structures become more stable than the 4×4-α structure for $\Delta\mu_{\mathrm{Si}} \leqslant -0.43$, -0.46, and -0.57 eV, respectively, the coexistence of which we propose as the origin of the T phase as discussed in Sec. III A 2. These structures are always less stable than the $\sqrt{13} \times \sqrt{13}$ type-IIα and β structures and are expected to readily change to more stable ones. This is also in agreement with the experimental fact that the T phase appears only at lower temperature and disappear by annealing.

The structure of the phase diagram can be modified by applying a strain to the system. Figure 5(b) shows the phase diagram of silicene on Ag(111) with a biaxial tensile strain of $+1\%$, where the most stable structures under the Si-poor, Si-rich, and intermediate conditions remain to be the $\sqrt{13} \times \sqrt{13}$ type-IIα, $2\sqrt{3} \times 2\sqrt{3}$-$\alpha$, and 4×4-α structures, respectively. As compared with Fig. 5(a), the $\sqrt{13} \times \sqrt{13}$ ($2\sqrt{3} \times 2\sqrt{3}$) structures are destabilized (stabilized) relative to the 4×4-α structure, which results in the phase boundaries at lower chemical potentials of $\Delta\mu_{\mathrm{Si}} = -0.49$ and 0.27 eV. Opposite behaviors can be seen in the phase diagram of silicene on Ag(111) with a biaxial compressive strain of -1% as shown in Fig. 5(c). Namely, the $\sqrt{13} \times \sqrt{13}$ ($2\sqrt{3} \times 2\sqrt{3}$) structures are stabilized (destabilized) relative to the 4×4-α structure, and the phase boundaries appear at higher chemical potentials of $\Delta\mu_{\mathrm{Si}} = 0.01$ and 0.69 eV. These results indicate that the buckled structures realized in silicene on Ag(111) can be tuned by applying a tensile or compressive strain to the system. Moreover, Fig. 5(b) [5(c)] shows that a tensile (compressive) strain stabilizes (destabilizes) the $2\sqrt{3} \times 2\sqrt{3}$-$\beta$ structure relative to the $2\sqrt{3} \times 2\sqrt{3}$-$\alpha$ structure, which suggests that the ratio of these structures is also tunable.

C. Electronic structures

The structural difference in silicene on Ag(111) influences its electronic properties and of particular importance is the existence of Dirac electrons, which is crucial for the realization of the quantum spin Hall effect. The existence of Dirac electrons has theoretically been predicted for alternately buckled freestanding silicene, while the 4×4-γ structure found in Sec. III A 1 has an analogous structure except for two Si atoms in a unit cell. Motivated by the similarity, we here investigate the electronic properties of the 4×4 structures shown in Fig. 1. The results for the other structures are given in the Supplemental Material [100]. To focus on the contribution from silicene, we plot in Fig. 6(a) the calculated energy bands of the 4×4-α structure weighted by the k-resolved DOS

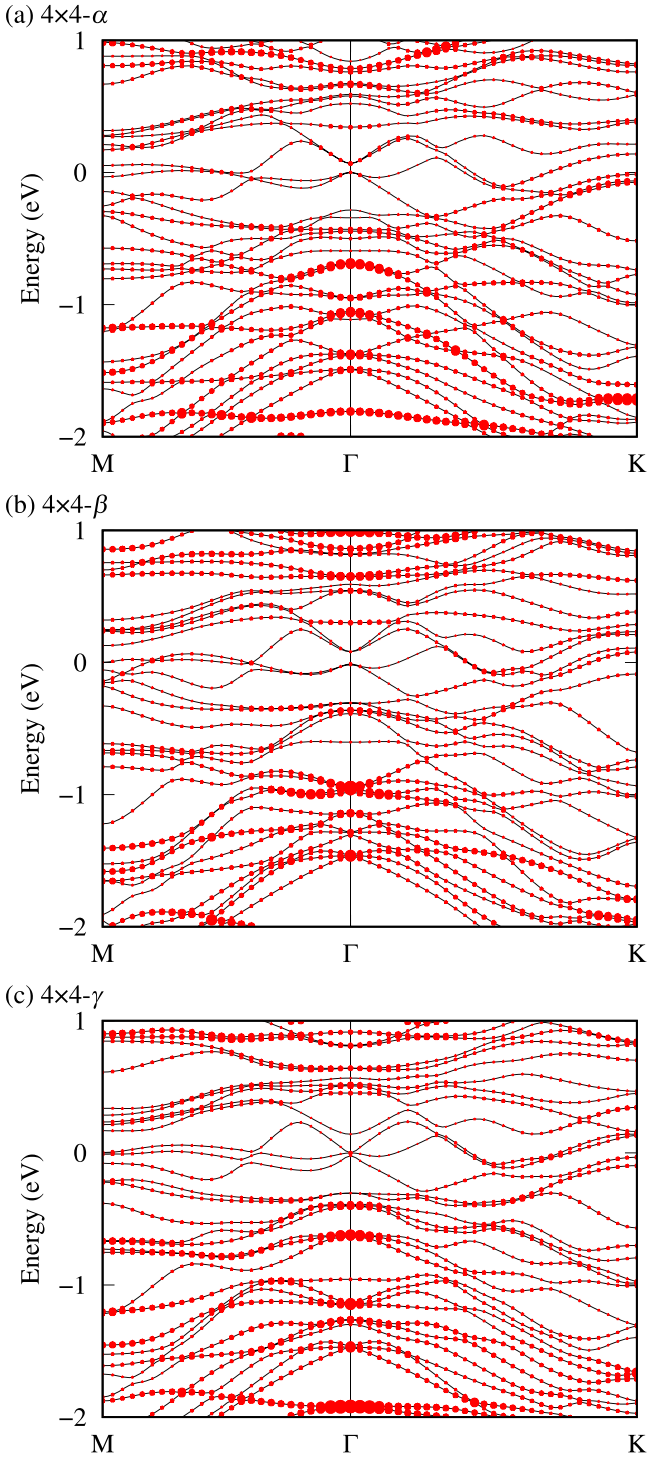

FIG. 6. The energy band diagrams of the 4×4-α (a), β (b), and γ (c) structures weighted by the k-resolved density of states (DOS) projected onto the silicene layer. The weight of the projected DOS is represented by the radius of a circle.

projected onto the silicene layer. Here the weight of the projected DOS is represented by the radius of a circle. Although a K point of the BZ of silicene-(1×1) is folded onto the Γ point of the BZ of Ag(111)-(4×4), no clear sign of linear bands derived from silicene can be observed near the Fermi level (E_F) at the Γ point. Instead, a π band is found to be $E_F - 0.95$ eV at the Γ point. These results indicate strong hybridization between silicene and the surface and are consistent with those of prior DFT calculations [34,64–69,73]. The absence of Dirac cones and the lowering of a silicene-derived π band can also be seen in the calculated energy bands of the 4×4-β structure as shown in Fig. 6(b). Note that the π band is found at the same energy as in Fig. 6(a) at the Γ point, although the details of the silicene-derived bands are significantly different from each other. Finally, we plot the calculated energy bands of the 4×4-γ structure in Fig. 6(c), which also show the absence of silicene-derived Dirac cones, despite the similarity of the buckled structure to freestanding silicene. This suggests that the hybridization with the surface states plays a more important role than the buckled structure of silicene in the disappearance of Dirac cones. Moreover, a silicene-derived π band is found at higher energy of $E_F - 0.62$ eV than in Figs. 6(a) and 6(b). We attribute this to the fact that fewer Si atoms in Fig. 1(c) contribute to the covalent bonds with the surface than those in Figs. 1(a) and 1(b).

IV. CONCLUSION

We have applied GOFEE to the search for the stable structures of silicene on Ag(111), and demonstrated that the method can not only reproduce the most stable structures but also predict metastable ones. It is found that there exist metastable structures that are close in stability to the most stable ones and can be observed experimentally. Such metastable structures play crucial roles in the stabilization of the less-ordered structures observed in the $\sqrt{13} \times \sqrt{13}$ type-II and $2\sqrt{3} \times 2\sqrt{3}$ phases. We have also identified the existence of the $\sqrt{13} \times \sqrt{13}$ type-I structures with monomer, dimer, and trimer protrusions, which are close in stability with each other. The coexistence of these structures can be considered the origin of the T phase, which has been experimentally observed as a mixture of round or elongated protrusions.

The fact that GOFEE has successfully generated a variety of stable structures of silicene on Ag(111) indicates that the method is also applicable to the investigation of other materials with nontrivial structures. In relation to two-dimensional materials, an intriguing example is a Ge monolayer grown on Ag(111). The system exhibits $7\sqrt{7} \times 7\sqrt{7}R19.1^\circ$ [101,102] and $\sqrt{109} \times \sqrt{109}R24.5^\circ$ [103] reconstructions commonly characterized by a hexamer protrusion, the details of whose structures are still controversial. Very recently, Zhang *et al.* have proposed models that explain these superstructures, in which the Ge monolayer contains a small amount of Ag atoms and consists of pentagonal, hexagonal, and heptagonal structures [103]. A large-scale GOFEE search is useful for elucidating the details of the alloy superstructures, and the obtained results will be discussed elsewhere.

ACKNOWLEDGMENTS

Y.H. and T.N.P. acknowledge financial support from Aarhus University and Elements Strategy Initiative for Catalysts and Batteries (ESICB), Kyoto University, and from the Innovative Professional Development (IPD) Program of the Professional Development Consortium for Computational Materials Scientists (PCoMS), respectively, for the stay at Aarhus University. The present study was supported by Grant-in-Aid for Scientific Research (C) (Grant No. JP21K03419) and a Research Fellowship for Young Scientists (DC) (Grant No. JP21J10648) from the Japan Society for the Promotion of Science (JSPS), by VILLUM FONDEN (Investigator Grant, Project No. 16562), and by the Danish National Research Foundation through the Center of Excellence "InterCat" (Grant Agreement No. DNRF150). The numerical calculations in this work were done using the facilities of the Supercomputer Center, Institute for Solid State Physics, University of Tokyo, and those of Cybermedia Center, Osaka University.

[1] K. V. Larionov and P. B. Sorokin, Investigation of atomically thin films: State of the art, Phys. Usp. **64**, 28 (2021).

[2] J. Si, J. Yu, Y. Shen, M. Zeng, and L. Fu, Elemental 2D materials: Progress and perspectives toward unconventional structures, Small Struct. **2**, 2000101 (2021).

[3] F. Bechstedt, P. Gori, and O. Pulci, Beyond graphene: Clean, hydrogenated and halogenated silicene, germanene, stanene, and plumbene, Prog. Surf. Sci. **96**, 100615 (2021).

[4] M. Yang, Z. Ye, M. A. Iqbal, H. Liang, and Y.-J. Zeng, Progress on two-dimensional binary oxide materials, Nanoscale **14**, 9576 (2022).

[5] K. A. Lozovoy, I. I. Izhnin, A. P. Kokhanenko, V. V. Dirko, V. P. Vinarskiy, A. V. Voitsekhovskii, O. I. Fitsych, and N. Y. Akimenko, Single-element 2D materials beyond graphene: Methods of epitaxial synthesis, Nanomaterials **12**, 2221 (2022).

[6] Q. Zhao, Z. Xie, Y.-P. Peng, K. Wang, H. Wang, X. Li, H. Wang, J. Chen, H. Zhang, and X. Yan, Current status and prospects of memristors based on novel 2D materials, Mater. Horiz. **7**, 1495 (2020).

[7] C. Grazianetti and C. Martella, The rise of the xenes: From the synthesis to the integration processes for electronics and photonics, Materials **14**, 4170 (2021).

[8] A. McCreary, O. Kazakova, D. Jariwala, and Z. Y. A. Balushi, An outlook into the flat land of 2D materials beyond graphene: Synthesis, properties and device applications, 2D Mater. **8**, 013001 (2021).

[9] Y. Liu, C. Zeng, Z. Jiahong, D. Junnan, Z. M. Wang, and L. Zongwen, Spintronics in two-dimensional materials, Nano-Micro Lett. **12**, 93 (2020).

[10] A. Avsar, H. Ochoa, F. Guinea, B. Özyilmaz, B. J. van Wees, and I. J. Vera-Marun, Colloquium: Spintronics in graphene and other two-dimensional materials, Rev. Mod. Phys. **92**, 021003 (2020).

[11] G. Hu and B. Xiang, Recent advances in two-dimensional spintronics, Nanoscale Res. Lett. **15**, 226 (2020).

[12] T. Wang, H. Wang, Z. Kou, W. Liang, X. Luo, F. Verpoort, Y.-J. Zeng, and H. Zhang, Xenes as an emerging 2D monoelemental family: Fundamental electrochemistry and energy applications, Adv. Funct. Mater. **30**, 2002885 (2020).

[13] M. B. Tahir and U. Fatima, Recent trends and emerging challenges in two-dimensional materials for energy harvesting and storage applications, Energy Storage **4**, e244 (2022).

[14] G. Khandelwal, S. Deswal, D. Shakthivel, and R. Dahiya, Recent developments in 2D materials for energy harvesting applications, J. Phys.: Energy **5**, 032001 (2023).

[15] C.-C. Liu, W. Feng, and Y. Yao, Quantum spin Hall effect in silicene and two-dimensional germanium, Phys. Rev. Lett. **107**, 076802 (2011).

[16] C.-C. Liu, H. Jiang, and Y. Yao, Low-energy effective Hamiltonian involving spin-orbit coupling in silicene and two-dimensional germanium and tin, Phys. Rev. B **84**, 195430 (2011).

[17] J. Zhuang, X. Xu, G. Peleckis, W. Hao, S. X. Dou, and Y. Du, Silicene: A promising anode for lithium-ion batteries, Adv. Mater. **29**, 1606716 (2017).

[18] A. Molle, C. Grazianetti, L. Tao, D. Taneja, M. H. Alam, and D. Akinwande, Silicene, silicene derivatives, and their device applications, Chem. Soc. Rev. **47**, 6370 (2018).

[19] Y. An, Y. Tian, C. Wei, Y. Zhang, S. Xiong, J. Feng, and Y. Qian, Recent advances and perspectives of 2D silicon: Synthesis and application for energy storage and conversion, Energy Storage Mater. **32**, 115 (2020).

[20] K. Takeda and K. Shiraishi, Theoretical possibility of stage corrugation in Si and Ge analogs of graphite, Phys. Rev. B **50**, 14916 (1994).

[21] S. Cahangirov, M. Topsakal, E. Aktürk, H. Şahin, and S. Ciraci, Two- and one-dimensional honeycomb structures of silicon and germanium, Phys. Rev. Lett. **102**, 236804 (2009).

[22] Y. Ding and J. Ni, Electronic structures of silicon nanoribbons, Appl. Phys. Lett. **95**, 083115 (2009).

[23] H. Şahin, S. Cahangirov, M. Topsakal, E. Bekaroglu, E. Akturk, R. T. Senger, and S. Ciraci, Monolayer honeycomb structures of group-IV elements and III-V binary compounds: First-principles calculations, Phys. Rev. B **80**, 155453 (2009).

[24] N. Y. Dzade, K. O. Obodo, S. K. Adjokatse, A. C. Ashu, E. Amankwah, C. D. Atiso, A. A. Bello, E. Igumbor, S. B. Nzabarinda, J. T. Obodo, A. O. Ogbuu, O. E. Femi, J. O. Udeigwe, and U. V. Waghmare, Silicene and transition metal based materials: Prediction of a two-dimensional piezomagnet, J. Phys.: Condens. Matter **22**, 375502 (2010).

[25] M. Houssa, G. Pourtois, V. V. Afanas'ev, and A. Stesmans, Can silicon behave like graphene? A first-principles study, Appl. Phys. Lett. **97**, 112106 (2010).

[26] C.-L. Lin, R. Arafune, K. Kawahara, N. Tsukahara, E. Minamitani, Y. Kim, N. Takagi, and M. Kawai, Structure of silicene grown on Ag(111), Appl. Phys. Express **5**, 045802 (2012).

[27] H. Jamgotchian, Y. Colignon, N. Hamzaoui, B. Ealet, J. Y. Hoarau, B. Aufray, and J. P. Bibérian, Growth of silicene layers on Ag(111): Unexpected effect of the substrate temperature, J. Phys.: Condens. Matter **24**, 172001 (2012).

[28] P. Vogt, P. De Padova, C. Quaresima, J. Avila, E. Frantzeskakis, M. C. Asensio, A. Resta, B. Ealet, and G. Le Lay, Silicene: Compelling experimental evidence for graphenelike two-dimensional silicon, Phys. Rev. Lett. **108**, 155501 (2012).

[29] B. Feng, Z. Ding, S. Meng, Y. Yao, X. He, P. Cheng, L. Chen, and K. Wu, Evidence of silicene in honeycomb structures of silicon on Ag(111), Nano Lett. **12**, 3507 (2012).

[30] D. Chiappe, C. Grazianetti, G. Tallarida, M. Fanciulli, and A. Molle, Local electronic properties of corrugated silicene phases, Adv. Mater. **24**, 5088 (2012).

[31] J. Avila, P. D. Padova, S. Cho, I. Colambo, S. Lorcy, C. Quaresima, P. Vogt, A. Resta, G. L. Lay, and M. C. Asensio, Presence of gapped silicene-derived band in the prototypical (3×3) silicene phase on silver (111) surfaces, J. Phys.: Condens. Matter **25**, 262001 (2013).

[32] E. Cinquanta, E. Scalise, D. Chiappe, C. Grazianetti, B. van den Broek, M. Houssa, M. Fanciulli, and A. Molle, Getting through the nature of silicene: An sp^2–sp^3 two-dimensional silicon nanosheet, J. Phys. Chem. C **117**, 16719 (2013).

[33] R. Arafune, C.-L. Lin, K. Kawahara, N. Tsukahara, E. Minamitani, Y. Kim, N. Takagi, and M. Kawai, Structural transition of silicene on Ag(111), Surf. Sci. **608**, 297 (2013).

[34] C.-L. Lin, R. Arafune, K. Kawahara, M. Kanno, N. Tsukahara, E. Minamitani, Y. Kim, M. Kawai, and N. Takagi, Substrate-induced symmetry breaking in silicene, Phys. Rev. Lett. **110**, 076801 (2013).

[35] G. Prévot, R. Bernard, H. Cruguel, and Y. Borensztein, Monitoring Si growth on Ag(111) with scanning tunneling microscopy reveals that silicene structure involves silver atoms, Appl. Phys. Lett. **105**, 213106 (2014).

[36] Z.-L. Liu, M.-X. Wang, J.-P. Xu, J.-F. Ge, G. L. Lay, P. Vogt, D. Qian, C.-L. Gao, C. Liu, and J.-F. Jia, Various atomic structures of monolayer silicene fabricated on Ag(111), New J. Phys. **16**, 075006 (2014).

[37] Z.-L. Liu, M.-X. Wang, C. Liu, J.-F. Jia, P. Vogt, C. Quaresima, C. Ottaviani, B. Olivieri, P. De Padova, and G. L. Lay, The fate of the $2\sqrt{3} \times 2\sqrt{3}R(30^\circ)$ silicene phase on Ag(111), APL Mater. **2**, 092513 (2014).

[38] N. W. Johnson, P. Vogt, A. Resta, P. De Padova, I. Perez, D. Muir, E. Z. Kurmaev, G. Le Lay, and A. Moewes, The metallic nature of epitaxial silicene monolayers on Ag(111), Adv. Funct. Mater. **24**, 5253 (2014).

[39] C. Grazianetti, D. Chiappe, E. Cinquanta, G. Tallarida, M. Fanciulli, and A. Molle, Exploring the morphological and electronic properties of silicene superstructures, Appl. Surf. Sci. **291**, 109 (2014).

[40] C. Grazianetti, D. Chiappe, E. Cinquanta, M. Fanciulli, and A. Molle, Nucleation and temperature-driven phase transitions of silicene superstructures on Ag(111), J. Phys.: Condens. Matter **27**, 255005 (2015).

[41] R. Bernard, Y. Borensztein, H. Cruguel, M. Lazzeri, and G. Prévot, Growth mechanism of silicene on Ag(111) determined by scanning tunneling microscopy measurements and *ab initio* calculations, Phys. Rev. B **92**, 045415 (2015).

[42] J. Zhuang, X. Xu, Y. Du, K. Wu, L. Chen, W. Hao, J. Wang, W. K. Yeoh, X. Wang, and S. X. Dou, Investigation of electron-phonon coupling in epitaxial silicene by *in situ* Raman spectroscopy, Phys. Rev. B **91**, 161409(R) (2015).

[43] C.-L. Lin, R. Arafune, M. Kawai, and N. Takagi, Comparison of electronic structure between monolayer silicenes on Ag(111), Chinese Phys. B **24**, 087307 (2015).

[44] A. Curcella, R. Bernard, Y. Borensztein, A. Resta, M. Lazzeri, and G. Prévot, Determining the atomic structure of the (4 × 4) silicene layer on Ag(111) by combined grazing-incidence x-ray diffraction measurements and first-principles calculations, Phys. Rev. B **94**, 165438 (2016).

[45] A. Díaz Álvarez, T. Zhu, J. Nys, M. Berthe, M. Empis, J. Schreiber, B. Grandidier, and T. Xu, Scanning tunnelling spectroscopy and Raman spectroscopy of monolayer silicene on Ag(111), Surf. Sci. **653**, 92 (2016).

[46] Y. Feng, D. Liu, B. Feng, X. Liu, L. Zhao, Z. Xie, Y. Liu, A. Liang, C. Hu, Y. Hu, S. He, G. Liu, J. Zhang, C. Chen, Z. Xu, L. Chen, K. Wu, Y.-T. Liu, H. Lin, Z.-Q. Huang, C.-H. Hsu, F.-C. Chuang, A. Bansil, and X. J. Zhou, Direct evidence of interaction-induced Dirac cones in a monolayer silicene/Ag(111) system, Proc. Natl. Acad. Sci. USA **113**, 14656 (2016).

[47] P. M. Sheverdyaeva, S. K. Mahatha, P. Moras, L. Petaccia, G. Fratesi, G. Onida, and C. Carbone, Electronic states of silicene allotropes on Ag(111), ACS Nano **11**, 975 (2017).

[48] Y. Oh, Y. Cho, H. Kwon, J. Lee, I. Jeon, W. Ko, H. W. Kim, J. Ku, G. Kim, H. Suh, and S. W. Hwang, Electronic structure and switching behavior of the metastable silicene domain boundary, Appl. Phys. Lett. **110**, 263112 (2017).

[49] M. R. Tchalala, H. Enriquez, A. J. Mayne, A. Kara, G. Dujardin, and H. Oughaddou, First steps of silicene growth on Ag(111), J. Phys.: Conf. Ser. **1081**, 012005 (2018).

[50] B. Feng, H. Zhou, Y. Feng, H. Liu, S. He, I. Matsuda, L. Chen, E. F. Schwier, K. Shimada, S. Meng, and K. Wu, Superstructure-induced splitting of Dirac cones in silicene, Phys. Rev. Lett. **122**, 196801 (2019).

[51] M. R. Tchalala, H. Enriquez, H. Yildirim, A. Kara, A. J. Mayne, G. Dujardin, M. A. Ali, and H. Oughaddou, Atomic and electronic structures of the $(\sqrt{13} \times \sqrt{13})R13.9^\circ$ of silicene sheet on Ag(111), Appl. Surf. Sci. **303**, 61 (2014).

[52] H. Jamgotchian, B. Ealet, H. Maradj, J.-Y. Hoarau, J.-P. Bibérian, and B. Aufray, A comprehensive analysis of the $(\sqrt{13} \times \sqrt{13})R13.9^\circ$ type II structure of silicene on Ag(111), J. Phys.: Condens. Matter **28**, 195002 (2016).

[53] B. Lalmi, H. Oughaddou, H. Enriquez, A. Kara, S. Vizzini, B. Ealet, and B. Aufray, Epitaxial growth of a silicene sheet, Appl. Phys. Lett. **97**, 223109 (2010).

[54] W. Wang, W. Olovsson, and R. I. G. Uhrberg, Experimental and theoretical determination of σ bands on ("$2\sqrt{3} \times 2\sqrt{3}$") silicene grown on Ag(111), Phys. Rev. B **92**, 205427 (2015).

[55] H. Jamgotchian, B. Ealet, Y. Colignon, H. Maradj, J.-Y. Hoarau, J.-P. Biberian, and B. Aufray, A comprehensive study of the $(2\sqrt{3} \times 2\sqrt{3})R30^\circ$ structure of silicene on Ag(111), J. Phys.: Condens. Matter **27**, 395002 (2015).

[56] Z. Majzik, M. R. Tchalala, M. Švec, P. Hapala, H. Enriquez, A. Kara, A. J. Mayne, G. Dujardin, P. Jelínek, and H. Oughaddou, Combined AFM and STM measurements of a silicene sheet grown on the Ag(111) surface, J. Phys.: Condens. Matter **25**, 225301 (2013).

[57] A. Resta, T. Leoni, C. Barth, A. Ranguis, C. Becker, T. Bruhn, P. Vogt, and G. Le Lay, Atomic structures of silicene layers grown on Ag(111): Scanning tunneling microscopy and noncontact atomic force microscopy observations, Sci. Rep. **3**, 2399 (2013).

[58] J. Onoda, K. Yabuoshi, H. Miyazaki, and Y. Sugimoto, High-resolution imaging of silicene on an Ag(111) surface by atomic force microscopy, Phys. Rev. B **96**, 241302(R) (2017).

[59] L. Feng, K. Yabuoshi, Y. Sugimoto, J. Onoda, M. Fukuda, and T. Ozaki, Structural identification of silicene on the Ag(111) surface by atomic force microscopy, Phys. Rev. B **98**, 195311 (2018).

[60] J. Onoda, L. Feng, K. Yabuoshi, and Y. Sugimoto, Less-ordered structures of silicene on Ag(111) surface revealed by atomic force microscopy, Phys. Rev. Mater. **3**, 104002 (2019).

[61] R. Pawlak, C. Drechsel, P. D'Astolfo, M. Kisiel, E. Meyer, and J. I. Cerda, Quantitative determination of atomic buckling of silicene by atomic force microscopy, Proc. Natl. Acad. Sci. USA **117**, 228 (2020).

[62] H. Enriquez, S. Vizzini, A. Kara, B. Lalmi, and H. Oughaddou, Silicene structures on silver surfaces, J. Phys.: Condens. Matter **24**, 314211 (2012).

[63] J. Gao and J. Zhao, Initial geometries, interaction mechanism and high stability of silicene on Ag(111) surface, Sci. Rep. **2**, 861 (2012).

[64] Z.-X. Guo, S. Furuya, J.-i. Iwata, and A. Oshiyama, Absence of Dirac electrons in silicene on Ag(111) surfaces, J. Phys. Soc. Jpn. **82**, 063714 (2013).

[65] Z.-X. Guo, S. Furuya, J.-I. Iwata, and A. Oshiyama, Absence and presence of Dirac electrons in silicene on substrates, Phys. Rev. B **87**, 235435 (2013).

[66] Y.-P. Wang and H.-P. Cheng, Absence of a Dirac cone in silicene on Ag(111): First-principles density functional calculations with a modified effective band structure technique, Phys. Rev. B **87**, 245430 (2013).

[67] P. Gori, O. Pulci, F. Ronci, S. Colonna, and F. Bechstedt, Origin of Dirac-cone-like features in silicon structures on Ag(111) and Ag(110), J. Appl. Phys. **114**, 113710 (2013).

[68] S. Cahangirov, M. Audiffred, P. Tang, A. Iacomino, W. Duan, G. Merino, and A. Rubio, Electronic structure of silicene on Ag(111): Strong hybridization effects, Phys. Rev. B **88**, 035432 (2013).

[69] P. Pflugradt, L. Matthes, and F. Bechstedt, Silicene-derived phases on Ag(111) substrate versus coverage: *Ab initio* studies, Phys. Rev. B **89**, 035403 (2014).

[70] M. Houssa, B. van den Broek, E. Scalise, B. Ealet, G. Pourtois, D. Chiappe, E. Cinquanta, C. Grazianetti, M. Fanciulli, A. Molle, V. Afanas'ev, and A. Stesmans, Theoretical aspects of graphene-like group IV semiconductors, Appl. Surf. Sci. **291**, 98 (2014).

[71] C. Lian and S. Meng, Dirac cone pairs in silicene induced by interface Si-Ag hybridization: A first-principles effective band study, Phys. Rev. B **95**, 245409 (2017).

[72] H. Liu, N. Han, and J. Zhao, Temperature and coverage effects on the stability of epitaxial silicene on Ag(111) surfaces, Appl. Surf. Sci. **409**, 97 (2017).

[73] J.-I. Iwata, Y.-I. Matsushita, H. Nishi, Z.-X. Guo, and A. Oshiyama, Mining single-electron spectra of the interface states from a supercell band structure of silicene on an Ag(111) substrate with band-unfolding methodology, Phys. Rev. B **96**, 235442 (2017).

[74] M. K. Bisbo and B. Hammer, Efficient global structure optimization with a machine-learned surrogate model, Phys. Rev. Lett. **124**, 086102 (2020).

[75] M. K. Bisbo and B. Hammer, Global optimization of atomic structure enhanced by machine learning, Phys. Rev. B **105**, 245404 (2022).

[76] M.-P. V. Christiansen, N. Rønne, and B. Hammer, Atomistic global optimization X: A Python package for optimization of atomistic structures, J. Chem. Phys. **157**, 054701 (2022).

[77] Z. Tang and B. Hammer, Dimerization of dehydrogenated polycyclic aromatic hydrocarbons on graphene, J. Chem. Phys. **156**, 134703 (2022).

[78] L. R. Merte, M. K. Bisbo, I. Sokolović, M. Setvín, B. Hagman, M. Shipilin, M. Schmid, U. Diebold, E. Lundgren, and B. Hammer, Structure of an ultrathin oxide on $Pt_3Sn(111)$ solved by machine learning enhanced global optimization, Angew. Chem. Int. Edit. **61**, e202204244 (2022).

[79] J. E. Quinlivan Domínguez, K. M. Neyman, and A. Bruix, Stability of oxidized states of freestanding and ceria-supported PtO_x particles, J. Chem. Phys. **157**, 094709 (2022).

[80] J. J. Mortensen, L. B. Hansen, and K. W. Jacobsen, Real-space grid implementation of the projector augmented wave method, Phys. Rev. B **71**, 035109 (2005).

[81] J. Enkovaara, C. Rostgaard, J. J. Mortensen, J. Chen, M. Dułak, L. Ferrighi, J. Gavnholt, C. Glinsvad, V. Haikola, H. A. Hansen, H. H. Kristoffersen, M. Kuisma, A. H. Larsen, L. Lehtovaara, M. Ljungberg, O. Lopez-Acevedo, P. G. Moses, J. Ojanen, T. Olsen, V. Petzold, N. A. Romero, J. Stausholm-Møller, M. Strange, G. A. Tritsaris, M. Vanin, M. Walter, B. Hammer, H. Häkkinen, G. K. H. Madsen, R. M. Nieminen, J. K. Nørskov, M. Puska, T. T. Rantala, J. Schiøtz, K. S. Thygesen, and K. W. Jacobsen, Electronic structure calculations with GPAW: A real-space implementation of the projector augmented-wave method, J. Phys.: Condens. Matter **22**, 253202 (2010).

[82] J. P. Perdew, K. Burke, and M. Ernzerhof, Generalized gradient approximation made simple, Phys. Rev. Lett. **77**, 3865 (1996).

[83] Y. S. Touloukian, R. K. Kirby, R. E. Taylor, and P. D. Desai, *Thermal Expansion—Metallic Elements and Alloys*, Thermophysical Properties of Matter Vol. 12 (IFI/Plenum, New York, 1975), p. 298.

[84] G. I. Csonka, J. P. Perdew, A. Ruzsinszky, P. H. T. Philipsen, S. Lebègue, J. Paier, O. A. Vydrov, and J. G. Ángyán, Assessing the performance of recent density functionals for bulk solids, Phys. Rev. B **79**, 155107 (2009).

[85] M. Satta, S. Colonna, R. Flammini, A. Cricenti, and F. Ronci, Silicon reactivity at the Ag(111) surface, Phys. Rev. Lett. **115**, 026102 (2015).

[86] STATE, https://state-doc.readthedocs.io (accessed Nov. 22, 2023).

[87] Y. Morikawa, K. Iwata, and K. Terakura, Theoretical study of hydrogenation process of formate on clean and Zn deposited Cu(111) surfaces, Appl. Surf. Sci. **169-170**, 11 (2001).

[88] Y. Morikawa, H. Ishii, and K. Seki, Theoretical study of *n*-alkane adsorption on metal surfaces, Phys. Rev. B **69**, 041403(R) (2004).

[89] N. Troullier and J. L. Martins, Efficient pseudopotentials for plane-wave calculations, Phys. Rev. B **43**, 1993 (1991).

[90] Y. Fukaya, I. Mochizuki, M. Maekawa, K. Wada, T. Hyodo, I. Matsuda, and A. Kawasuso, Structure of silicene on a Ag(111) surface studied by reflection high-energy positron diffraction, Phys. Rev. B **88**, 205413 (2013).

[91] D. Tsoutsou, E. Xenogiannopoulou, E. Golias, P. Tsipas, and A. Dimoulas, Evidence for hybrid surface metallic band in (4×4) silicene on Ag(111), Appl. Phys. Lett. **103**, 231604 (2013).

[92] P. Moras, T. O. Mentes, P. M. Sheverdyaeva, A. Locatelli, and C. Carbone, Coexistence of multiple silicene phases in silicon grown on Ag(111), J. Phys.: Condens. Matter **26**, 185001 (2014).

[93] M. S. Rahman, T. Nakagawa, and S. Mizuno, Growth of Si on Ag(111) and determination of large commensurate unit cell of high-temperature phase, Jpn. J. Appl. Phys. **54**, 015502 (2015).

[94] S. Mahatha, P. Moras, P. Sheverdyaeva, V. Bellini, T. Menteş, A. Locatelli, R. Flammini, K. Horn, and C. Carbone, Absence of Dirac cones in monolayer silicene and multilayer Si films on Ag(111), J. Electron Spectrosc. **219**, 2 (2017).

[95] A. Curcella, R. Bernard, Y. Borensztein, A. Resta, M. Lazzeri, and G. Prévot, Structure and stability of silicene on Ag(111) reconstructions from grazing incidence x-ray diffraction and density functional theory, Phys. Rev. B **99**, 205411 (2019).

[96] H. Enriquez, A. Kara, A. J. Mayne, G. Dujardin, H. Jamgotchian, B. Aufray, and H. Oughaddou, Atomic structure of the $(2\sqrt{3} \times 2\sqrt{3})R30^\circ$ of silicene on Ag(111) surface, J. Phys.: Conf. Ser. **491**, 012004 (2014).

[97] M. Dion, H. Rydberg, E. Schröder, D. C. Langreth, and B. I. Lundqvist, Van der Waals density functional for general geometries, Phys. Rev. Lett. **92**, 246401 (2004).

[98] J. Klimeš, D. R. Bowler, and A. Michaelides, Van der Waals density functionals applied to solids, Phys. Rev. B **83**, 195131 (2011).

[99] K. Reuter and M. Scheffler, Composition, structure, and stability of $RuO_2(110)$ as a function of oxygen pressure, Phys. Rev. B **65**, 035406 (2001).

[100] See Supplemental Material at http://link.aps.org/supplemental/10.1103/PhysRevMaterials.7.124002 for the energy band diagrams calculated for the other structures of silicene on the Ag(111) surface.

[101] J. Yuhara, H. Shimazu, K. Ito, A. Ohta, M. Araidai, M. Kurosawa, M. Nakatake, and G. Le Lay, Germanene epitaxial growth by segregation through Ag(111) thin films on Ge(111), ACS Nano **12**, 11632 (2018).

[102] S. Mizuno, A. Ohta, T. Suzuki, H. Kageshima, J. Yuhara, and H. Hibino, Correlation between structures and vibration properties of germanene grown by Ge segregation, Appl. Phys. Express **14**, 125501 (2021).

[103] K. Zhang, M.-C. Hanf, R. Bernard, Y. Borensztein, H. Cruguel, A. Resta, Y. Garreau, A. Vlad, A. Coati, D. Sciacca, B. Grandidier, M. Derivaz, C. Pirri, P. Sonnet, R. Stephan, and G. Prévot, The ground state of epitaxial germanene on Ag(111), ACS Nano **17**, 15687 (2023).